Volume 7
Number 8
21 April 2023
Pages 1759–2014

Sustainable Energy & Fuels

Interdisciplinary research for the development of sustainable energy technologies

rsc.li/sustainable-energy

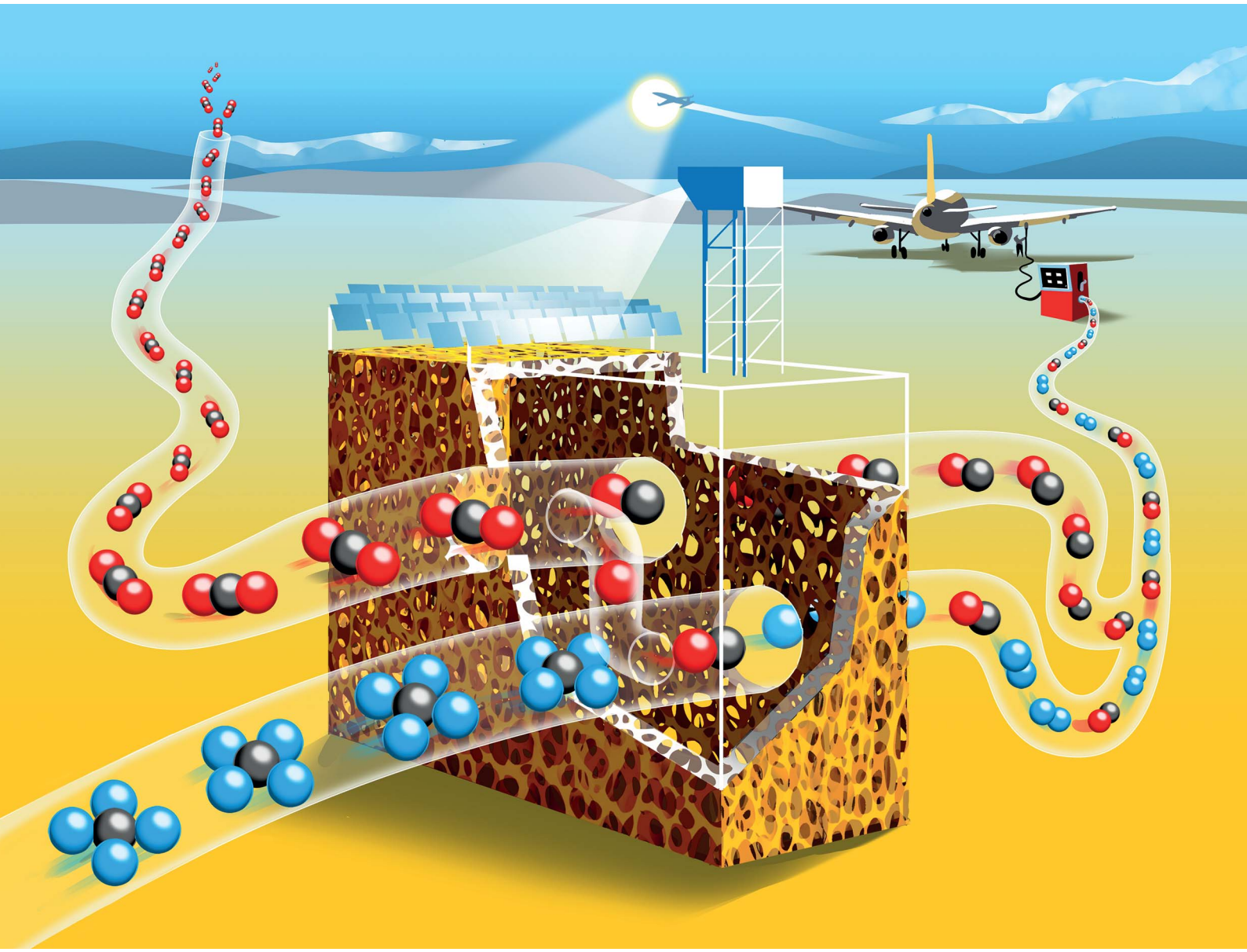

ISSN 2398-4902

ROYAL SOCIETY OF CHEMISTRY

PAPER
Aldo Steinfeld *et al.*
Methane dry reforming *via* a ceria-based redox cycle in a concentrating solar tower

Sustainable Energy & Fuels

ROYAL SOCIETY OF CHEMISTRY

PAPER

View Article Online
View Journal | View Issue

Cite this: *Sustainable Energy Fuels*, 2023, **7**, 1804

Methane dry reforming *via* a ceria-based redox cycle in a concentrating solar tower

Mario Zuber,[a] Moritz Patriarca,[ab] Simon Ackermann,[b] Philipp Furler,[b] Ricardo Conceição,[c] José Gonzalez-Aguilar,[c] Manuel Romero[c] and Aldo Steinfeld *[a]

Drop-in fuels produced using solar energy can provide a viable pathway towards sustainable transportation, especially for the long-haul aviation sector which is strongly dependent on jet fuel. This study reports on the experimental testing of a solar reactor using concentrated solar energy for the production of syngas, a mixture of mainly H_2 and CO, which serves as the precursor for the synthesis of kerosene and other liquid hydrocarbon fuels. The thermochemical conversion route is based on the dry reforming of CH_4 *via* a 2-step redox cyclic process utilizing the intermediation of non-sacrificial ceria (CeO_2), comprising: (1) the endothermal reduction of $CeO_{2-\delta_{ox}}$ with CH_4 to form $CeO_{2-\delta_{red}}$ and syngas (δ denoting the non-stoichiometry); and (2) the exothermal oxidation of $CeO_{2-\delta_{red}}$ with CO_2 to form CO and the oxidized state of $CeO_{2-\delta_{ox}}$. The solar reactor consists of a cavity-receiver lined with a reticulated porous ceramic (RPC) structure and an axial tubular section at the cavity's rear filled with a packed-bed of agglomerates, both RPC and agglomerates made of pure ceria. Testing is performed at a high-flux solar tower at conditions and scale relevant to industrial implementation. For a solar radiative power input of 10 kW (corresponding to a mean solar flux of 560 suns) at temperatures in the range 800–1000 °C, with reacting gas flow rates of 105 normal L min^{-1} and concentrations of CH_4 (reduction step) and CO_2 (oxidation step) of up to 20% in Ar, the solar-driven redox reforming process yields a peak CH_4 molar conversion of 70% and a peak H_2 selectivity of 68%. Co-feeding of CH_4 and CO_2 during the reduction step resulted in the highest solar-to-fuel energy efficiency of 27%, defined as the ratio of the higher heating value of the syngas produced over the sum of the solar radiative power input through the solar reactor's aperture and the higher heating value of CH_4 fed to the solar reactor. Regardless of the operational mode, the syngas product composition was similar at equal δ attained during the reduction. The addition of the tubular packed bed increased the syngas yield by 32%.

Received 14th December 2022
Accepted 17th February 2023

DOI: 10.1039/d2se01726a

rsc.li/sustainable-energy

Introduction

Solar thermochemical processes driven by concentrated solar radiation utilize the entire solar spectrum as the source of high-temperature process heat and therefore offer a thermodynamically efficient pathway to the synthesis of sustainable fuels.[1] Of particular interest is the solar thermochemical production of syngas – a specific mixture of mainly H_2 and CO which can be further processed to synthesize drop-in fuels for transportation, and in particular solar kerosene for long-haul aviation.[2,3] Syngas can be produced by solar-driven reforming, which has been extensively studied.[4–12] The catalytic reforming of CH_4 with CO_2 (dry) or H_2O (wet) is represented by the net reactions:

Dry reforming:

$$CH_4(g) + CO_2(g) \rightarrow 2CO(g) + 2H_2(g) \quad \Delta H^{\circ}_{298\,K} = 247\ \text{kJ mol}^{-1} \tag{R1}$$

Wet reforming:

$$CH_4(g) + H_2O(g) \rightarrow CO(g) + 3H_2(g) \quad \Delta H^{\circ}_{298\,K} = 206\ \text{kJ mol}^{-1} \tag{R2}$$

Both reactions are highly endothermic and proceed at temperatures above 600 °C. Relevant side reactions are the Boudouard ($2CO \rightarrow CO_2 + C(s)$) and methane decomposition ($CH_4 \rightarrow 2H_2 + C(s)$), both resulting in carbon formation, and the reverse water-gas shift (RWGS: $H_2 + CO_2 \rightarrow H_2O + CO$), which affects the syngas quality.[13] An additional concern is catalyst deactivation due to oxidation, thermal sintering, and/or carbon deposition.[13]

Syngas can be also produced from H_2O and CO_2 *via* a 2-step thermochemical redox cycle using metal oxides.[14] Ceria (CeO_2)

[a]*ETH Zurich, Department of Mechanical and Process Engineering, 8092 Zurich, Switzerland. E-mail: aldo.steinfeld@ethz.ch*
[b]*Synhelion SA, Via Cantonale 19, 6900 Lugano, Switzerland*
[c]*High-Temperature Processes Unit, IMDEA Energy, E-28935 Móstoles, Spain*

is an attractive metal oxide for such a cycle because of its stability and rapid kinetics.[15–17] The H_2O/CO_2-splitting redox cycle based on ceria is represented by:

Reduction:

$$\frac{1}{\Delta\delta}CeO_{2-\delta_{ox}} \rightarrow \frac{1}{\Delta\delta}CeO_{2-\delta_{red}} + \frac{1}{2}O_2 \quad (R3)$$

Oxidation with CO_2:

$$\frac{1}{\Delta\delta}CeO_{2-\delta_{red}} + CO_2 \rightarrow \frac{1}{\Delta\delta}CeO_{2-\delta_{ox}} + CO \quad (R4)$$

Oxidation with H_2O:

$$\frac{1}{\Delta\delta}CeO_{2-\delta_{red}} + H_2O \rightarrow \frac{1}{\Delta\delta}CeO_{2-\delta_{ox}} + H_2 \quad (R5)$$

δ denotes the non-stoichiometry – the measure of the redox extent. Ceria is not consumed but undergoes consecutive redox cycles. The redox cycle is operated under a temperature-swing mode and/or a pressure-swing mode to control the oxygen exchange capacity of ceria $\Delta\delta = \delta_{red} - \delta_{ox}$, and thereby the fuel yield per cycle and per mole of metal oxides. Typically, the reduction step is performed at 1500 °C and 10 mbar and the oxidation step at 900 °C and 1 bar, for which $\Delta\delta \approx 0.03$.[16] These temperature and pressure swings impose severe thermal and mechanical stresses on the solar reactor materials. In contrast, the catalytic reforming process (R1 and R2) proceeds at more moderate and constant temperatures but at the expense of introducing a carbonaceous fuel (CH_4) which undergoes partial oxidation. Of particular interest is the methanothermal reduction of ceria through the combination of the two aforementioned routes for syngas production, namely the catalytic reforming ((R1) and (R2), and the H_2O/CO_2-splitting redox cycle R3–R5), into the so-called "dry/wet redox reforming" cyclic process,[15,18–25] represented by:

Reduction:

$$\frac{1}{\Delta\delta}CeO_{2-\delta_{ox}} + CH_4 \rightarrow \frac{1}{\Delta\delta}CeO_{2-\delta_{red}} + CO + 2H_2 \quad (R6)$$

Oxidation with CO_2 (dry):

$$\frac{1}{\Delta\delta}CeO_{2-\delta_{red}} + CO_2 \rightarrow \frac{1}{\Delta\delta}CeO_{2-\delta_{ox}} + CO \quad (R7)$$

Oxidation with H_2O (wet):

$$\frac{1}{\Delta\delta}CeO_{2-\delta_{red}} + H_2O \rightarrow \frac{1}{\Delta\delta}CeO_{2-\delta_{ox}} + H_2 \quad (R8)$$

This cyclic process operates in an isobaric and isothermal manner, thus eliminating the temperature and pressure swings of the H_2O/CO_2-splitting redox cycle. Furthermore, higher non-stoichiometric ranges are possible ($\Delta\delta \lessapprox 0.345$) at significantly lower and more feasible temperatures ($\approx$1000 °C), thus acting as a bridge technology to the H_2O/CO_2-splitting redox cycle.[26,27]

A recent thermodynamic analysis comparing the conventional catalytic reforming with the redox reforming highlights a favorable selectivity and tunable syngas composition of the latter approach, but at the expense of additional thermodynamic constraints which are sensitive to carbon formation and lead to a greater energy demand relative to catalytic reforming.[27] A relevant unwanted reaction for the redox reforming process is the complete oxidation of CH_4 which occurs at low non-stoichiometries of the reduced form of ceria (*e.g.* $\delta_{red} \lessapprox 0.05$ at 1000 °C):

$$\frac{4}{\Delta\delta}CeO_{2-\delta_{ox}} + CH_4 \rightarrow \frac{4}{\Delta\delta}CeO_{2-\delta_{red}} + CO_2 + 2H_2O \quad (R9)$$

At low δ, ceria can be more easily reduced; as is often seen when initially reducing fully oxidized ceria. Thus, operating at higher δ results in improved syngas selectivity and higher H_2 : CO ratios during reduction, as well as improved CO_2 conversion during oxidation. The high δ range combined with the dependence of the product composition on δ elucidate the importance of defining reduced (δ_{red}) and oxidized (δox) states of ceria. In (R6), CH_4 serves as reducing agent of the metal oxide, as previously proposed for the co-production of metals and syngas using solar process heat.[28–30] The redox reforming process can also be performed by co-feeding H_2O and/or CO_2. The CeO_2 remains active and its state is affected by the feeding molar ratios $H_2O:CH_4$ and $CO_2:CH_4$ until equilibrium is reached (δ_{eq}). CeO_2 has often been employed to act as a basic catalyst support which improves CO_2 adsorption and promotes the RWGS.[13] It further enhances reducibility, oxygen mobility, material stability, and is resistant to deactivation *via* sintering at high temperatures.[13,31–33]

Four reviews summarize the solar reactor developments.[34–37] Solar reactor concepts applied for the redox reforming process include particle-flow transport,[20] a vortex-flow reactor,[38] a tubular packed bed,[39,40] a tubular array with bi-directional flow,[24] and a cavity-receiver containing a foam-type structure.[18,41–43] A cavity-receiver lined with a reticulated porous ceramic (RPC) structure made of ceria has been previously applied for the H_2O/CO_2-splitting redox cycle with a 4 kW solar reactor in a solar dish concentrator,[2] and with a 50 kW solar reactor in a solar tower.[3] In this study, we employ a modified version of that solar reactor concept to perform the dry redox reforming cyclic process (R6 and R7), with and without co-feeding of CO_2 in the reduction step. Focus is on this process as it supports complete dry reforming due to ceria's oxygen exchange properties, offers high selectivity, improves the syngas quality required for downstream Fischer–Tropsch synthesis, and contributes to the technology development for the H_2O/CO_2-splitting redox cycle with purely thermal reduction (R3). Furthermore, the use of CO_2 as oxidizing agent provides a path for producing carbon-neutral drop-in fuels, provided CO_2 is derived from a biogenic source of captured from the air.[2] The study highlights the use of ceria as redox material for solar reforming in a coupled (*i.e.* cavity) and decoupled (*i.e.* packed bed) solar receiver-reactor, operated in cyclic or co-feeding modes. Experimentation is carried out in a solar tower with

a heliostat field, which offers a platform for on-sun testing the solar reactor and its peripheral components at conditions and scale relevant to industrial implementation.

Solar reactor and experimental setup

Solar concentrating system

The experimental campaign was conducted at the solar tower facility of IMDEA Energy in Móstoles, Spain.[3,44] It consists of a solar field with 169 heliostats, each with a facet area of ≈3 m^2, which track the sun and concentrate the direct normal solar irradiance (DNI) onto the solar reactor located at the top of a 15 m solar tower. The entire heliostat field was designed to supply a solar radiative power of 250 kW for a DNI ≈850 W m^{-2} at equinox noon. The experimental campaign used an average of 38 heliostats, which resulted in a mean solar concentration ratio of 560 suns, delivering approximately 10 kW into the 160 mm dia. aperture of the solar reactor.

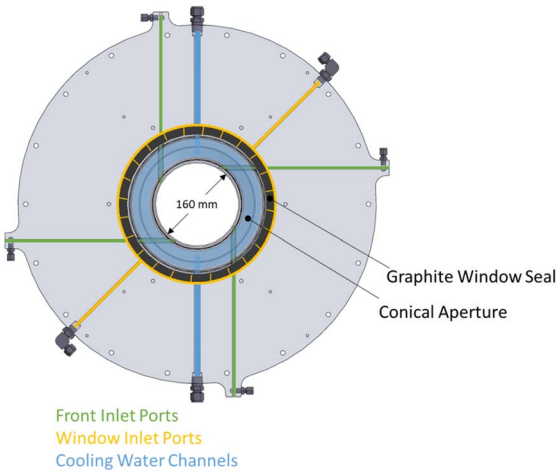

Fig. 2 Front of solar reactor in a transparent view detailing the two main gas inlet ports: the front inlet port (green) for reactive and inert gases, and the window inlet port (yellow) for inert gases. The cooling water channel (blue) prevents the conical aperture from overheating.

Solar reactor design

The solar reactor is shown schematically in Fig. 1. The main design features are highlighted here. It consists of a cavity-receiver with 160 mm dia. aperture sealed with a 12 mm thick quartz disk for the access of concentrated solar radiation. The inner cavity is lined with RPC bricks made of pure ceria, creating a 350 mm dia., 375 mm length near-cylindrical (hexadecagon) enclosure. With this arrangement, the RPC structure is directly exposed to the incoming concentrated solar flux, providing volumetric radiative absorption and efficient heat transfer directly to the reaction site.[45]

The actively cooled aluminum front serves as a shield from radiation spillage, and air jets provide active cooling on the quartz window. The steel cavity casing is lined with aluminum silicate insulation (Al_2O_3–SiO_2, Rath Inc., type KVS 184/400) behind the RPC bricks. Gases primarily enter the cavity *via* ports on the front (see Fig. 2), while a port on the steel casing allows for a safety bypass channel. (1) the front inlet port for reactive and inert gases injected tangential to and behind the aperture through four channels, thus creating a counter-clockwise (CCW) swirl as seen from the front; (2) the window inlet port for inert gas entering *via* grooves in the graphite seal located between the quartz window and aluminum front, which are angled at 25° to induce a CCW swirl; (3) the casing inlet port for inert gas preventing heating of upstream sensors and as a safety bypass channel in the event of overpressure.

Downstream to the cavity, the gases flow into the tubular section (95 mm dia., 500 mm length) which is lined with alumina and a ceramic fiber tube. This tubular section can be used as an additional redox material installation zone thus extending the residence time. Contrary to the vortex flow regime in the cavity, a plug flow regime with a low Reynolds number is characteristic of the tubular packed bed, whereby the reactant

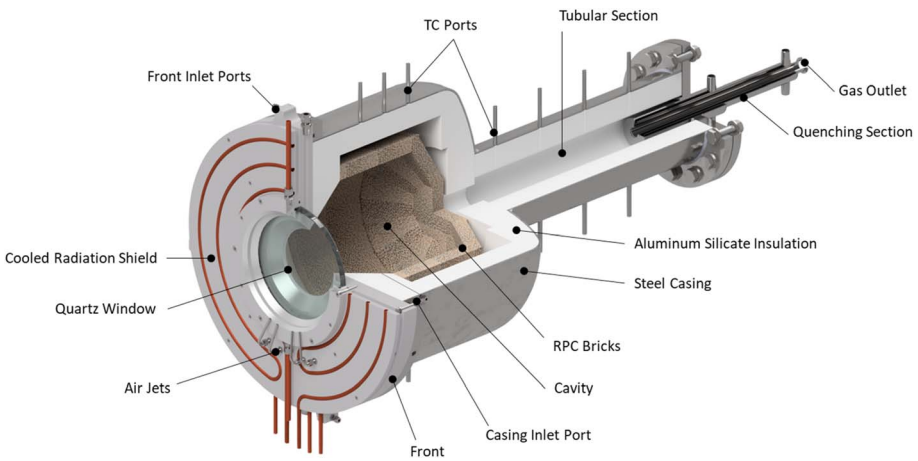

Fig. 1 Solar reactor configuration, consisting of a cavity-receiver with a windowed aperture containing a reticulated porous ceramic (RPC) structure made of ceria.

gases are forced to flow through the reactive material contrary to the cavity flow where only a fraction of the reactant gas flow may interact with the ceria. The packed bed increases the thermal mass and mimics the behaviour of a thermocline heat storage, allowing reactions to proceed even when P_{solar} is interrupted due to clouds. Finally, a quenching section rapidly cools the off-gas prior to entering the chemical analysis equipment.

Materials

Ceria (cerium(IV) oxide, CeO_2) is the redox material at the core of the solar reactor. There are two main installation zones for the redox material: the cavity and the tubular section, as depicted in Fig. 3, thus presenting the possibility for various loading configurations. The cavity contains ceria RPC bricks with dual-scale interconnected porosity in the mm and μm ranges for enhanced heat and mass transfer.[46] They are made by the replica method,[46] with 7 ppi (pores per inch) polyurethane (PU) foam, 27 vol% pore former content (PFC) using 150 μm cylindrical carbon fibers, and sintered at 1600 °C resulting in an effective density of 1.50 $cm^3\ g^{-1}$ and SSA (specific surface area) of 0.04 $m^2\ g^{-1}$ (measured by mercury intrusion porosimetry). The total mass of ceria RPC is 20.7 kg of roughly 34 mm thickness, with a total surface area of 828 m^2. The tubular section contains a packed bed of 8 mm mean dia. ceria agglomerates, formed with 27 vol% PFC of 150 μm cylindrical carbon fibers, sintered at 1100 °C, resulting in an SSA of 1.44 $m^2\ g^{-1}$ (measured by gas adsorption analysis and a Brunauer–Emmett–Teller measurement). The total mass of the packed bed is 4.5 kg which equates to a surface area of 6480 m^2, thus augmenting the kinetic rates. The agglomerate morphology does not have to absorb direct irradiation nor be self-supporting. Agglomerates were used because of their relatively high SSA and their overall fast kinetic rates obtained in preliminary lab tests with a packed-bed tubular reactor. Fig. 3 shows the scanning electron microscopy (SEM) images, detailing the microstructure of the RPC and agglomerates.

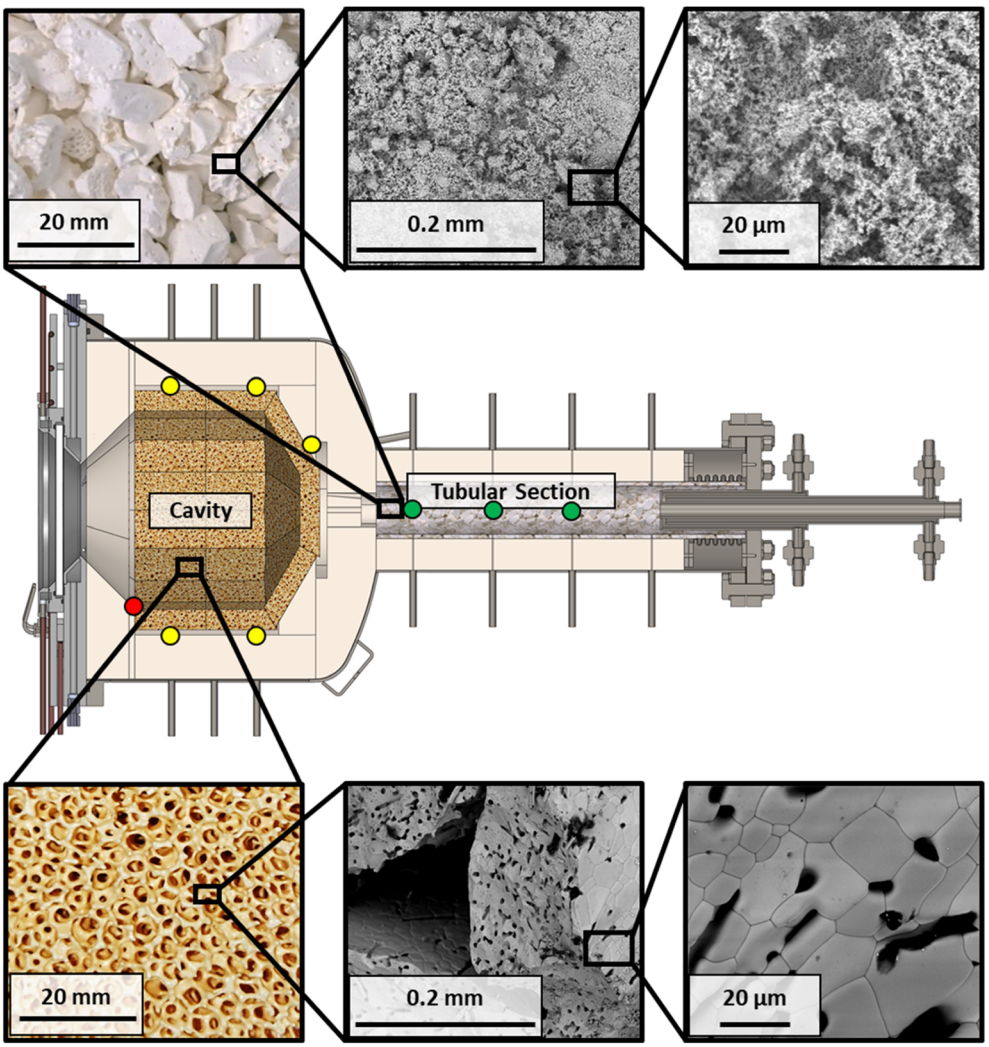

Fig. 3 Cross section of the solar reactor with two ceria installation zones, namely: the cavity and the tubular section. The cavity is lined with ceria RPC bricks. The tubular section is filled with a packed bed of ceria agglomerates. SEM images are shown detailing their microstructure. Thermocouples' locations are indicated by colored dots: B-type (yellow), K-type in cavity (red), K-type in the tubular section (green).

Experimental setup

The experimental setup, including the solar reactor, the feeding and handling of reactant and product gases, and the measurement instrumentation, is schematically shown in Fig. 4. The solar reactor is positioned on the top of the solar tower at the west operating position, and tilted 40° down towards the heliostat field. A water calorimeter is installed in the east operating position of the solar tower and is used to determine the solar radiative power input P_{solar} entering through the aperture of the solar reactor.[3,47] A radiative shield that moves in front of the solar reactor is used to block P_{solar}. Gas flows are controlled by mass flow controllers (MFC, Bronkhorst EL-FLOW Select). Pressure sensors (Leybold Thermovac, Gefran KS) are installed at each inlet and before the soot filter and the unidirectional check valve. B-Type thermocouples (TCs) are installed inside the cavity and K-Type TCs are positioned throughout the system to monitor cooling loops, surfaces, and outlet gas temperatures. The hot gas flowing out of the quenching section passes through metal tubes before reaching a soot filter and the final exhaust port. The gas analysis unit (ULTRAMAT 23 and CALOMAT 6, Siemens AG) is placed in parallel to the main outlet flow and draws in 1–2 L_n min^{-1} of gas (L_n denotes normal liters) through a condenser and filter (MAK 10 – AGT Thermotechnik GmbH & Co KG) to measure the concentrations of CO, CO_2, CH_4, and H_2. A mass flow meter (Bronkhorst EL-FLOW Select) is connected downstream to monitor the flow through the gas analysis unit and to ensure there are appropriate flow levels for accurate measurement of gas concentrations. Three video cameras are installed in the experimental area of the solar tower for live monitoring. Additional safety peripherals include a flashback arrestor, pressure controller, overpressure relief valves, ceiling mounted CH_4 and CO sensors, and an emergency shutdown located in the control room. The system is monitored and controlled from the control room *via* a system control and data acquisition system.

Experimental procedure

When the DNI >750 W m^{-2}, the solar cavity is heated up to the desired steady-state operating temperature in the range 800–1200 °C. Standard flows during an experimental run are 50 L_n min^{-1} argon (Ar) through the window inlet port (to act as a protective curtain), 50 L_n min^{-1} reacting gas mixture through the front inlet port, and 5 L_n min^{-1} Ar through the casing inlet port. Typical pressures in the cavity range between 900–1200 mbar. When carbon deposition is observed, testing is halted to reduce the chance of overpressure due to clogging, or window fracture. At the end of the run, the heliostats are defocused and the ceria is re-oxidized. The nominal cavity temperature, $T_{nominal}$, is defined as the average of all the B-Type TCs located in the cavity and touching the back of the RPCs (Fig. 3, yellow dots). The nominal packed bed temperature, $T_{pb,nominal}$, is defined as the average of all the K-Type TCs located in the tubular section (Fig. 3, green dots). The following performance indicators of the solar thermochemical fuel process are determined.[48]

The conversion of an educt, *i*, is given by:

$$X_i = \frac{n_{i,in} - n_{i,out}}{n_{i,in}} \quad (1)$$

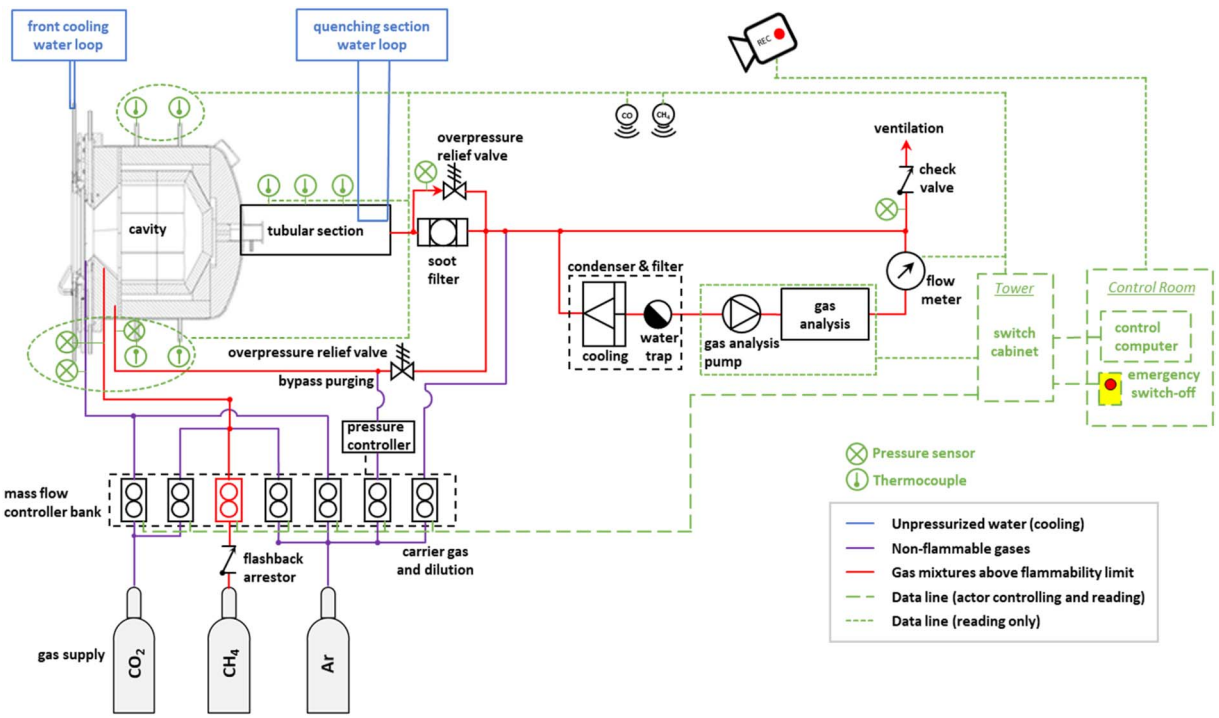

Fig. 4 Experimental setup at the solar tower of IMDEA Energy, depicting the solar reactor, the feeding and handling of reactant gases, and the measurement instrumentation.

The total moles in and out of the system are taken across a single cycle or time range. The selectivity of a product k describes how much of the converted educt i forms the desired product k, defined as:

$$S_k = \left|\frac{\nu_i}{\nu_k}\right| \frac{n_{k,\text{out}}}{n_{i,\text{in}} - n_{i,\text{out}}} \quad (2)$$

Eqn (1) and (2) define the instantaneous X_i and S_k. Since the process is transient by nature, the values of X_i and S_k are determined by integration over a complete cycle.

The change in δ of $CeO_{2-\delta}$ is based on the change in oxygen atoms between the products and educts (Δn_O), where the H_2O across a cycle or time range can be determined from a molar balance:

$$n_{H_2O,\text{out}} = 2\cdot(n_{CH_4,\text{in}} - n_{CH_4,\text{out}}) - 2\cdot n_{H_2,\text{out}} \quad (3)$$

$$\Delta n_O = n_{H_2O,\text{out}} + n_{CO,\text{out}} + 2\cdot n_{CO_2,\text{out}} - 2\cdot n_{CO_2,\text{in}} \quad (4)$$

$$\Delta\delta = \frac{\Delta n_O}{m_{\text{reactor loading}}/M_{CeO_2}} \quad (5)$$

The $\Delta\delta$ across a data point with an inert reactor was zero (*i.e.* $\Delta\delta = -6.35\cdot10^{-6}$), and corroborates the molar balance. The solar-to-fuel energy efficiency for the solar reactor is defined as the ratio of the high heating value of the syngas (H_2 and CO) to the total energy input into the reactor, *i.e.* the sum of Q_{solar} during both redox steps and the higher heating value of CH_4 injected during the reduction step:

$$\eta_{\text{solar-to-fuel}} = \frac{\text{HHV}_{H_2} n_{H_2,\text{out}} + \text{HV}_{CO} n_{CO,\text{out}}}{Q_{\text{solar}} + \text{HHV}_{CH_4} n_{CH_4,\text{in}}} \quad (6)$$

Note that this definition of energy efficiency refers to the performance of the solar reactor only; it does not consider the optical efficiency of the concentrating solar tower facility. Note also that $Q_{\text{solar}} = \int P_{\text{solar}} dt$ (over the duration of a cycle/run) and P_{solar} typically represented about 1/25 of the concentrated solar radiative power that theoretically can be delivered by the entire heliostat field.

Results and discussion

The experimental results were collected over 24 testing days. Throughout the entire testing campaign, the calorimeter was used to measure the solar radiative power input P_{solar} onto the reactor aperture (incident on the quartz window), which was curve fitted with respect to the number of heliostats pointing at the aperture, the DNI, and the average field cosine factors,[49] resulting in an accuracy of $\pm$ 2.0 kW based on a 90% confidence interval. Prior to testing with ceria, the solar reactor was tested with an inert cavity of alumina liner to prove the cavity can endure high flow rates of up to 300 L_n min^{-1} at $T_{\text{nominal}} = 1049$ °C. Multiple tests were also conducted with varying Ar flow distributions and seal angle configurations (*e.g.* 25° counterclockwise (CCW) or 0° causing no swirl) to elucidate the effect of the flow combinations on the fluid dynamics within the cavity. These experimental findings along with past studies investigating the effects of Reynolds and swirl numbers on window depositions motivated a flow configuration consisting of 50% through the reactor inlet and 50% through the window inlet using the 25°CCW seal for all subsequent testing to protect the window from depositions.[50] With this arrangement there was no evidence of dust depositions on the window for the redox reforming and co-feeding tests.

CH_4 cracking

Co-producing carbon and H_2 by thermal decomposition of CH_4 – also referred to as CH_4 cracking – can be seen as a bridge technology to a hydrogen economy,[51–53] and the solar-driven process has been studied experimentally.[54–56] However, in the present study, it is an unwanted reaction as the C from the CH_4 should go into producing CO. Furthermore, the CH_4 cracking reaction is detrimental for the operation of the solar reactor because carbon deposition can reduce the structural integrity of the window, induces pressure increase *via* clogging of downstream components, and as a consequence compromises the overall safety. The means of detecting CH_4 cracking in order of occurrence are: (1) carbon cloud or swirl seen at the aperture with the CCD (charge-coupled device) camera; (2) sharp temperature increase on the K-Type TC located in the cavity behind the aperture, attributed to radiative absorption by the carbon particle cloud; (3) observable carbon depositions on the

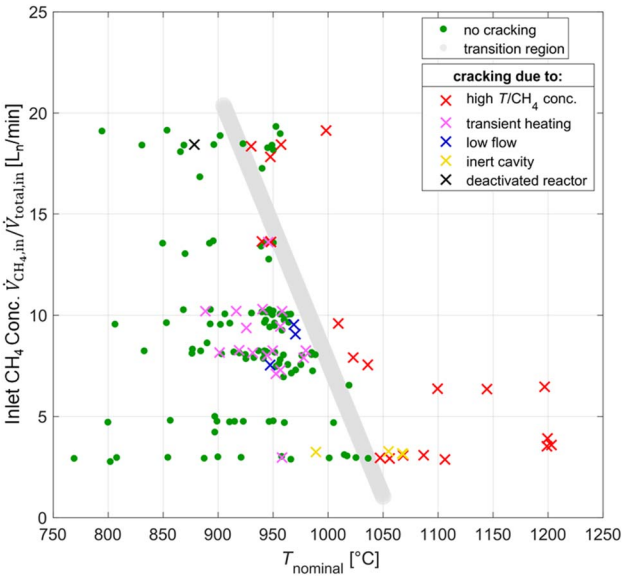

Fig. 5 Test map of operational parameters of inlet CH_4 concentration and T_{nominal} points. Standard conditions involve a flow rate at 105 L_n min^{-1} and a cavity lined with CeO_2 RPCs. A transition region (grey line) separates the conditions of no CH_4 cracking (green dots) from conditions that lead to CH_4 cracking (x). Conditions for cracking include too high temperatures or inlet CH_4 concentrations (red x), transient heating effects caused by heliostat additions or varying DNI (pink x), lower flow conditions (<105 L min^{-1}) (blue x), and an inert or deactivated ceria cavity which does not exchange oxygen for the partial oxidation of CH_4 (yellow/black x).

MAK 10 soot filter, viewed by video camera; (4) pressure increase due to clogging of downstream components; and (5) spike in the H_2 outlet concentration. Fig. 5 shows a test map of inlet CH_4 concentration and $T_{nominal}$ points, and details a transition region (indicated by the grey line) between instances with cracking (symbol x) and without cracking (symbol green dot). The experimental conditions that presumably caused CH_4 cracking were the relatively higher temperatures or inlet CH_4 concentrations (symbol red x), transient heating effects caused by heliostat additions or varying DNI (symbol pink x), lower flow conditions (<105 L min^{-1}) (symbol blue x), and an inert or deactivated ceria cavity which does not exchange oxygen for the partial oxidation of CH_4 (symbol yellow/black x). The deactivated ceria cavity occurred from a co-feed test in which transient heating caused CH_4-cracking and resulted in carbon depositions on the reactor cavity thus resulting in deactivation of the CeO_2 redox material. To oxidize all of the carbon depositions in the cavity and to reactivate the redox activity of the ceria, CO_2 was fed into the reactor at high concentrations (>40%) while ramping $T_{nominal}$ up to 1200 °C.

Redox reforming

The typical redox reforming cycle consists of a reduction step of 30 s and an oxidation step of 90 s separated by an inert step of 60 s where only Ar is injected. The short reduction times are chosen to prevent any local increase in δ that may cause a phase change at elevated δ ($\gtrapprox 0.25$) and can lead to mechanical instabilities, crystallographic changes, dampened thermodynamic properties, and/or barriers preventing stable redox cycles.[18,26,57–60] On the other hand, the oxidation step is typically set to a longer duration to ensure complete re-oxidation of the ceria structure. Another means of implementing the redox reforming cycle is *via* the high-δ scheme. This approach aims to take advantage of the improved syngas selectivity at higher δ. First, δ is increased either by injecting CH_4 or a mixture of CH_4 and CO_2. Then, the redox steps proceed during 60 s each by injecting CH_4 during reduction and CO_2 during oxidation to prevent a significant change in the δ regime. The solar radiative power input, nominal temperature, inlet/outlet gas compositions, and δ of $CeO_{2-\delta}$ are shown in Fig. 6 as a function of time during high-δ redox reforming cycles. The solar radiative input varied throughout the test due to DNI changes. The endothermicity of the reduction step and exothermicity of the oxidation step led to respective decrease and increase of $T_{nominal}$. During reduction, CO and H_2 (from R6), CO_2 and H_2O (from R9) and unconverted CH_4 were observed, while δ increased and the selectivity of CO and H_2 followed. During oxidation, unconverted CO_2 and CO (from R7) were observed, while δ decreased and higher CO_2 conversions occurred at the higher values of δ.

A parametric study was performed for the redox reforming cycles in the range 800–1000 °C (isothermal for both redox steps) and for inlet reacting gas concentrations of 3, 5, 10, and 20% CH_4-Ar during the reduction step and 3, 5, 10, and 20% CO_2-Ar during the oxidation step (same concentrations of CH_4 and CO_2 for the same cycle), using a total flow of 105 L_n min^{-1}. Different flow rates and flow configurations were tested during the commissioning stage to find the optimal configuration for uniform flow distribution within the cavity and for preventing backflow and possible carbon depositions on the quartz window. Inlet reacting gas concentrations were ramped up to determine the feasibility of running such a system under conditions closely matching industrial operation. The reactor was monitored for carbon depositions at each testing interval. Note that the residence time was not an experimental parameter

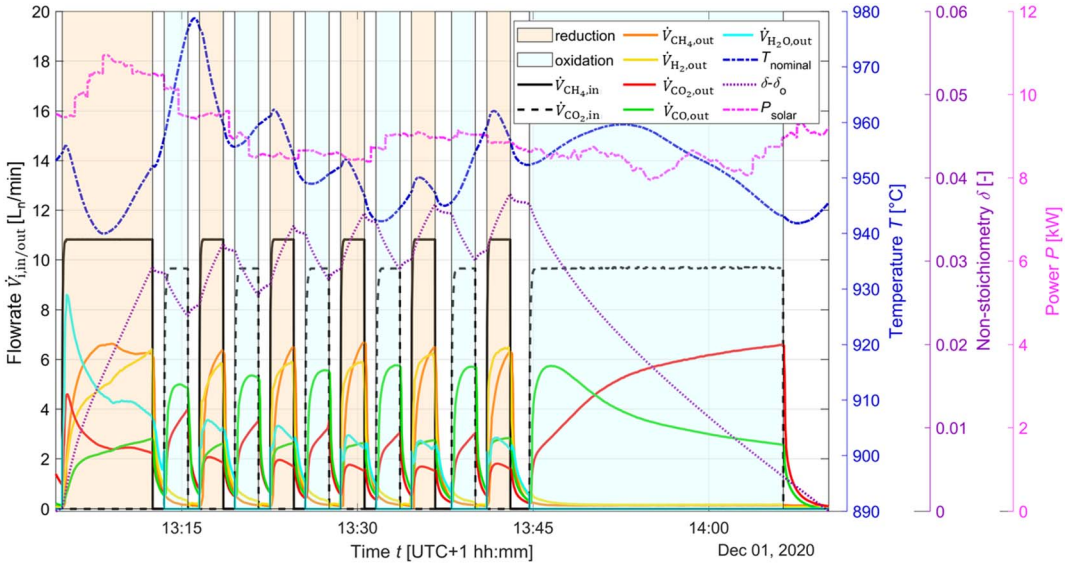

Fig. 6 Solar radiative power input, nominal temperature, inlet/outlet gas compositions, and δ of $CeO_{2-\delta}$ as a function of time during high-δ redox reforming cycles. Flow rate data was smoothed using a local regression with weighted linear least squares and a 2nd degree polynomial. H_2O flowrate data was determined *via* C : H ratio balance. To illustrate the high-δ cycles, the $\delta - \delta_o$ plot is adjusted with the start point as δ_o and the subsequent values are linearly and uniformly shifted to ensure $\delta_{end} - \delta_o \approx 0$. In reality, $\delta_{end} = 0.038$ due to a gradual shift over the cycling.

for controlling coking because it was practically fixed for the optimal flow configuration. Three cycles were performed at each parameter point (the average of which is reported) to ensure reproducibility and approximate steady-state conditions, determined by minimal variation in the product composition between cycles. The initial reduction step and final oxidation step during high-δ redox reforming cycles are not included in the analysis. A few patterns observed in the results are attributed to the order of testing: from low to high gas concentrations and from low to high temperatures. Data points were collected

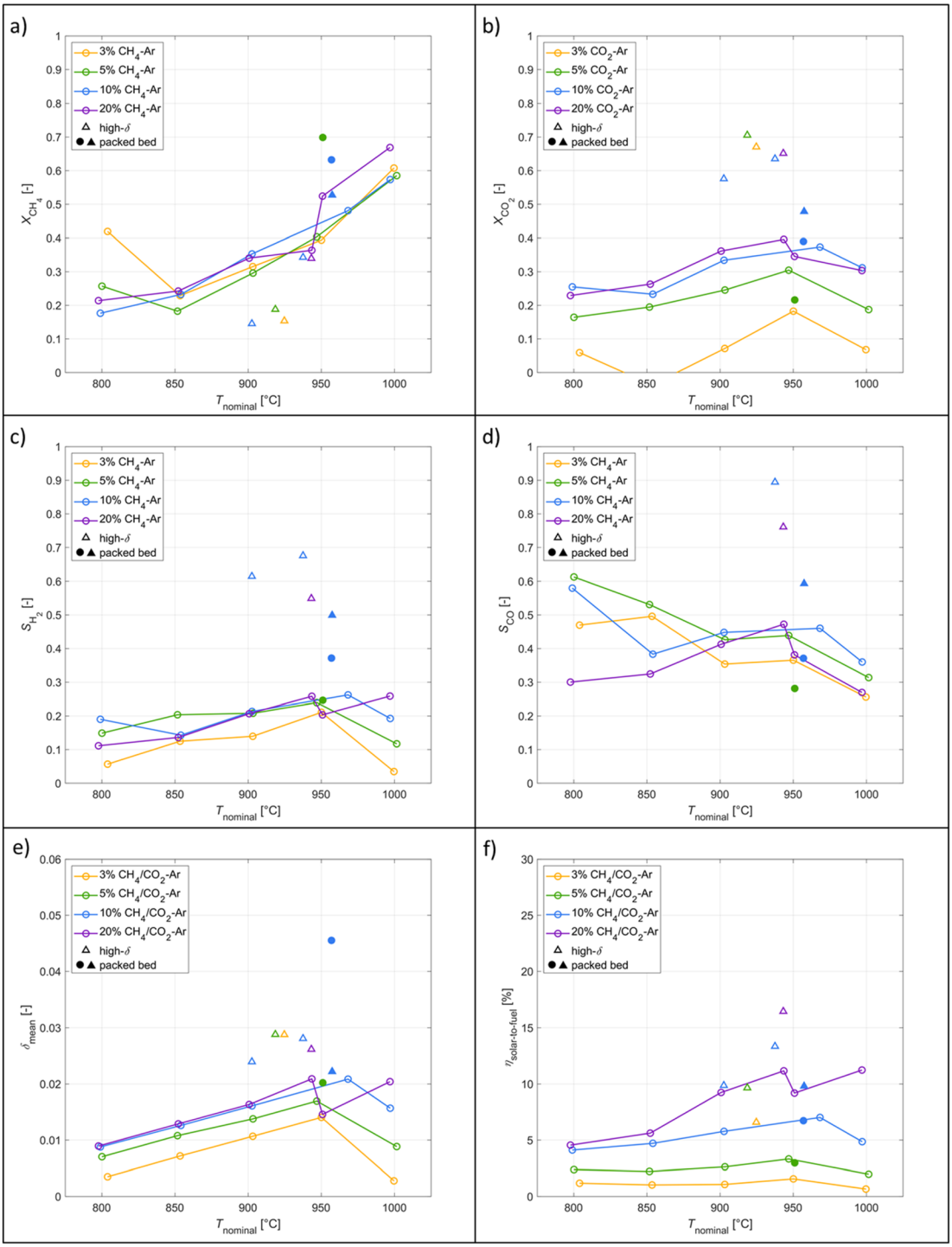

Fig. 7 Experimental results as a function of the nominal temperature for redox reforming cycles: (a) CH_4 molar conversion for the reduction step. (b) CO_2 molar conversion for the oxidation step. (c) H_2 selectivity of the reduction step. (d) CO selectivity of the reduction step. (e) Average δ of $CeO_{2-\delta}$ across a complete redox reforming cycle. (f) Solar-to-fuel energy efficiency. Tests were performed at varying inlet reacting gas concentrations (3%, 5%, 10%, 20%), high-δ cycles, and with the packed bed installation in the tubular section.

on the same day apart from the runs at 1000 °C and at 20% and 950 °C. A longer oxidation with 20% CO_2 occurred prior to the run at 850 °C, affecting the results. There was evidence of CH_4 cracking for the run at 20% and 1000 °C which is included in the analysis for completeness of the data set. A few patterns observed in the packed-bed data points are attributed to the relative testing time: the difference between $T_{nominal}$ and $T_{pb,nominal}$ ($\Delta T_{average} = 210$ °C) was highest at the start of testing ($\Delta T_{average} = 404$ °C), and lowest at the end of testing ($\Delta T_{average} = -14$ °C). Along the packed bed an axial temperature gradient of $\Delta T_{average} = 302$ °C was observed. Note that the RPCs remained in the cavity with the packed bed installation.

CH_4 and CO_2 molar conversions. The molar conversions of CH_4 (0.15–0.70) and CO_2 (0–0.71) for the reduction and oxidation steps are shown in Fig. 7a and b, respectively, as a function of the nominal temperature. The CH_4 conversion increased with temperature as predicted by thermodynamics.[27] No observable dependence on concentration, *i.e.* no plateau or decrease in the conversions, suggests the absence of kinetic limitations as well as enough redox active ceria within the cavity. The data point for the run at 3% and 800 °C appears to be an outlier and can be explained by the order of testing. The lower CH_4 conversion for the high-δ cycles is consistent with thermodynamic predictions,[27] and can be also partially attributed to CH_4 cracking occurring prior to these runs, thus resulting in the carbon depositions on the RPC and lower activity. On the other hand, CO_2 conversion increased at the higher testing δ ranges.[27] The data point for the run at 3% and 850 °C showed a negative conversion due to the previous long oxidation event. The data points obtained in the run performed on the separate day yielded lower CO_2 conversion due to the lower testing δ range. X_{CH_4} and X_{CO_2} were higher with the packed bed due to the additional CeO_2 in the system thus allowing for an increased residence time. The cycle at 5% and 950 °C had lower X_{CO_2} than the RPC cavity tests as it was affected by the relative testing time; it was the first test conducted on the day and the agglomerate was not reduced enough to be readily re-oxidized by CO_2.

H_2 and CO selectivities. The selectivities of H_2 (0.035–0.68) and CO (0.26–0.89) for the reduction step are shown in Fig. 7c and d, respectively, as a function of the nominal temperature. S_{H_2} increased with temperature due to the higher testing δ range. Thermodynamically (and if at equal δ) S_{H_2} should be higher at lower temperatures.[27] However, the opposite was observed due to limitations imposed by kinetics and lower CH_4 conversions at lower temperatures. The run at 20% and 1000 °C yielded a significantly higher S_{H_2} due to the CH_4 cracking. The trends in S_{CO} are not as clear due to transient flow effects from the preceding oxidation step and by the RWGS at lower δ. The high-δ data points indicate improved syngas selectivity as thermodynamics predict.[27] Analogously, the runs performed on the separate day show lower selectivities due to a lower testing δ range. The packed-bed resulted in higher S_{H_2} and commensurate S_{CO} to that of the RPC cavity tests. This was caused by the increased SSA which led to higher δ, and also allowed the reduction reaction to proceed at lower temperatures.

Mean non-stoichiometry. δ_{mean} of $CeO_{2-\delta}$ across a complete redox reforming cycle (0.0028–0.046) is shown as function of the nominal reaction temperature in Fig. 7e δ_{mean} increased with $T_{nominal}$ because of the higher CH_4 conversions (see Fig. 7a). Furthermore, δ_{mean} increased with concentration because of the higher amount of reacting gas to partake in reducing CeO_2. The high-δ tests showed higher δ_{mean} as intended and substantiated the operation setting of these cycles. The δ_{mean} on the separate day continued to increase as in the testing order, but decreased for the run at 950 °C due to the improved oxidation at higher δ and lower $T_{nominal}$. Analysis of $\Delta\delta$ across a reduction and oxidation steps provide evidence of the non-steady-state conditions ($\Delta\delta_{reduction} \gg \Delta\delta_{oxidation}$) for the runs at 1000 °C on the separate day. δ_{mean} values were higher with the packed bed as the additional CeO_2 with higher SSA improved the reaction rate.

Solar-to-fuel energy efficiency. $\eta_{solar\text{-}to\text{-}fuel}$ (0.66–16.4% ± 2.5%) as a function of the nominal reaction temperature is shown in Fig. 7f. Note that Q_{solar} for a complete cycle includes the solar radiative input during both redox steps but excludes the energy delivered during the inert Ar step. $\eta_{solar\text{-}to\text{-}fuel}$ increased with $T_{nominal}$ because of the higher CH_4 and CO_2 conversions (see Fig. 7a and b). Furthermore, $\eta_{solar\text{-}to\text{-}fuel}$ increased with concentration because of the higher δ and syngas quantity produced (in absolute terms), as expected due to improvements in selectivity and CO_2 conversion. $\eta_{solar\text{-}to\text{-}fuel}$ with the packed-bed showed improvement to that of the RPC cavity tests due to increased educt conversions and syngas selectivities.

Co-feeding CH_4 and CO_2

Experimental runs were performed by co-feeding CH_4 and CO_2, *i.e.* by combining the reduction and oxidation steps in one continuous feed flow, according to:

$$CH_4 + CO_2 \xrightarrow{CeO_{2-\delta_{red}}} 2CO + 2H_2 \quad (R10)$$

To determine the viability of continuously producing syngas in a single step similar to the catalytic dry reforming (R1). CO_2 and CH_4 were injected at a given $CO_2 : CH_4$ molar ratio, which is maintained above unity to prevent excessive ceria reduction. According to thermodynamics, a $CO_2 : CH_4 = 1.2 : 1$ at 950 °C corresponds to $\delta_{eq} \approx 0.12$. The solar radiative power input, nominal temperature, inlet/outlet gas composition, and δ of $CeO_{2-\delta}$ are shown in Fig. 8 as a function of time for the co-feeding run. Isothermal operation was easier to control than redox reforming due to continuous flow of reactants. The endothermicity of the reaction led to gradual decrease of $T_{nominal}$. During co-feeding, unconverted CH_4 and CO_2, and CO and H_2 (from R10), and H_2O from side reactions (*e.g.* RWGS, and R9) were observed. The δ reached a steady-state value. Note that long co-feeding runs produced significant delays in the system, as can be seen in the variation in the δ value after co-feeding.

The co-feeding runs were performed in the range 800–950 °C under standard total flow of 105 L_n min^{-1}, and reacting gas concentration of 40% with $CO_2 : CH_4 = 4 : 1$, $3 : 1$, $2 : 1$, and $1.2 : 1$. The data taken for subsequent analysis was obtained during

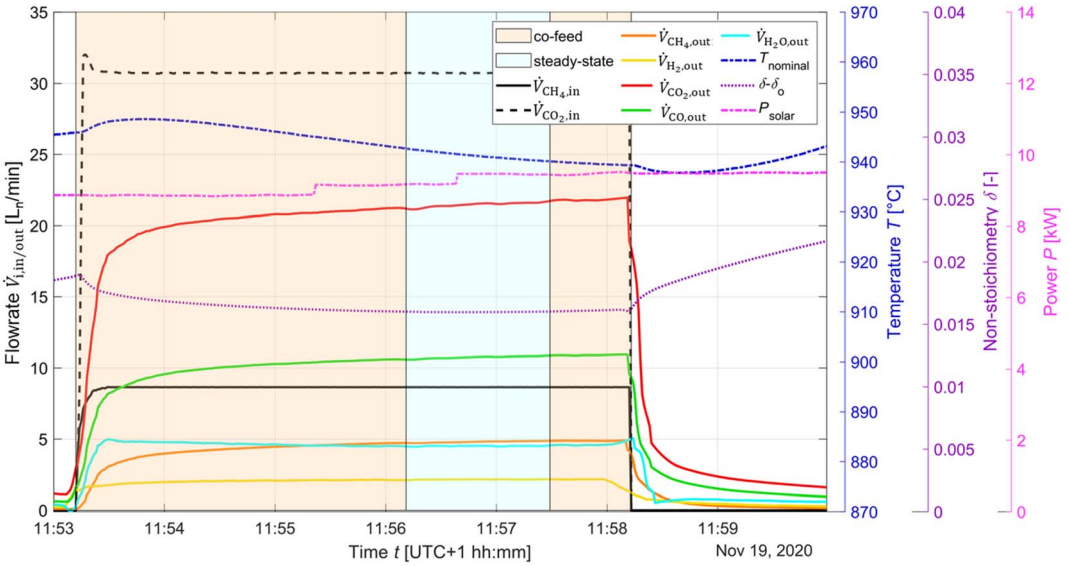

Fig. 8 Solar radiative power input, nominal temperature, inlet/outlet gas compositions, and δ of $CeO_{2-\delta}$ as a function of time for the co-feeding run. Flowrate data was smoothed using a local regression with weighted linear least squares and a 2nd degree polynomial. H_2O flow rate data was determined *via* C : H ratio balance.

approximate steady-state conditions assumed by stable product composition during roughly 200 s. Higher temperatures were not tested due to the risk of CH_4 cracking. A few patterns observed in the results are attributed to transient heating effects and the endothermicity of the reforming reaction, which have a notable effect on $T_{nominal}$ and on reaching steady-state conditions. Refer to the section on Redox reforming for the patterns observed in results with respect to the packed-bed.

CH_4 and CO_2 molar conversions. The molar conversions of CH_4 (0.063–0.59) and CO_2 (0.092–0.63) are shown in Fig. 9a and b, respectively, as a function of the nominal temperature for the co-feeding runs. Both conversions increased with temperature as the reforming reaction becomes more thermodynamically favourable.[27,34] As expected, the CO_2 conversion also increased with $CO_2 : CH_4$ molar ratio as a larger percentage of CO_2 can react with CH_4. On the contrary, the CH_4 conversion did not vary with $CO_2 : CH_4$ molar ratio suggesting another limitation such as the residence time. Analogous to the redox reforming, X_{CH_4} and X_{CO_2} were higher with the packed bed.

H_2 and CO selectivities. The selectivities of H_2 (0.19–0.71) and CO (0.69–0.99) for the co-feeding runs are shown in Fig. 9c and d, respectively, as a function of the nominal temperature. As S_{H_2} are thermodynamically expected to remain relatively constant over temperatures,[27] it is hypothesized that S_{H_2} increased with $T_{nominal}$ because of the faster kinetics to reach higher δ_{eq} and thus decreased the complete oxidation of CH_4 reaction (R9). Furthermore, S_{H_2} increased for lower $CO_2 : CH_4$ as there was less CO_2 in the system to drive the RWGS turning H_2 into H_2O. Analogous to the redox reforming, the packed bed resulted in higher S_{H_2} and commensurate S_{CO} to that of the RPC cavity tests.

Mean non-stoichiometry. δ_{mean} measured for the co-feeding runs (0.0064–0.057) is shown in Fig. 9e as a function of the nominal temperature. δ_{mean} approached the equilibrium δ_{eq} when steady-state was reached. As expected from thermodynamics, δ_{mean} increased with temperature due to increasing X_{CH_4} and decreasing favorability in re-oxidizing *via* CO_2.[27] Furthermore, δ_{mean} increased for lower values of $CO_2 : CH_4$ because of less excess CO_2 to oxidize ceria. Analysis of $\Delta\delta$ across the steady-state regime shows near zeros values indicating little change in the oxidation state of ceria. Slight deviation towards negative values are attributed to the endothermicity of the reforming reaction thus gradually decreasing $T_{nominal}$. δ_{mean} were higher with the packed bed as the additional CeO_2 with higher SSA improved the reaction rate. The co-feeding runs at 4 : 1 $CO_2 : CH_4$ at 937 °C and 3 : 1 $CO_2 : CH_4$ at 947 °C did not show this behaviour due to the relative testing time: these runs were conducted at the start of testing when the system was still heating up and yet to reach steady temperatures in the packed bed. The co-feeding runs at 2 : 1 $CO_2 : CH_4$ also did not show larger δ_{mean} values as these points were gathered after transient heating effects.

Solar-to-fuel energy efficiency. $\eta_{solar\text{-}to\text{-}fuel}$ (6.67–27.3% ± 2.5%) as a function of the nominal temperature obtained for the co-feeding runs is shown in Fig. 9f $\eta_{solar\text{-}to\text{-}fuel}$ increased with temperatures because of the higher educt conversions. In spite of the higher S_{H_2}, there is no clear improvement in $\eta_{solar\text{-}to\text{-}fuel}$ for higher values of $CO_2 : CH_4$, presumably because the endothermic reaction required more solar thermal energy to maintain a certain temperature. Furthermore, the syngas produced per mol of CH_4 is independent of $CO_2 : CH_4$ as the RWGS can convert the H_2 and the excess CO_2 in the product into H_2O and CO. Analogous to the redox reforming, $\eta_{solar\text{-}to\text{-}fuel}$ showed improvement with the packed-bed to that of the RPC cavity tests due to increased educt conversions and syngas selectivities. Comparing experimentally measured energy efficiencies of previous studies is challenging due to varying setups and definitions, and the lack of data to convert the reported values to

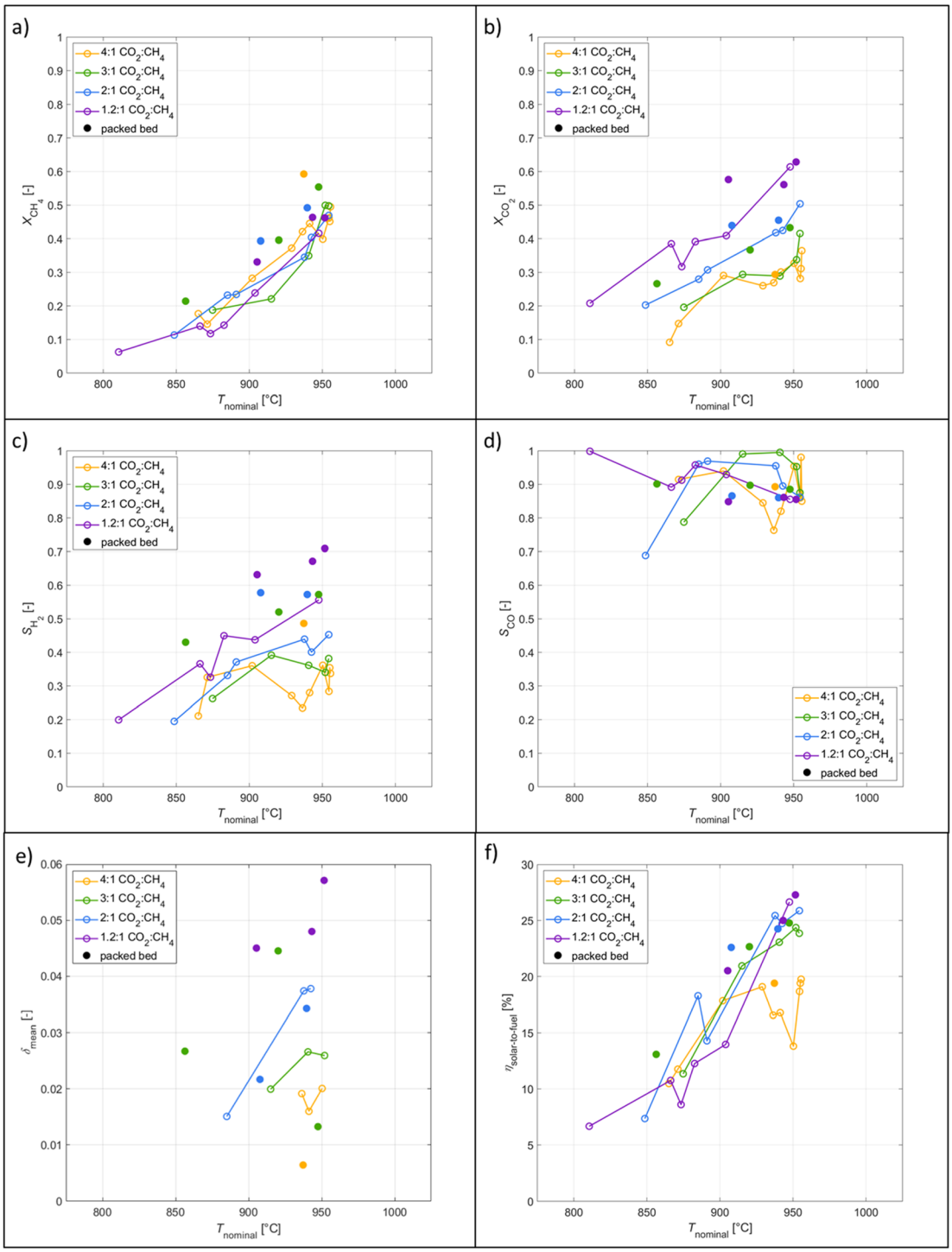

Fig. 9 Experimental results as a function of the nominal temperatures for the co-feeding runs: (a) CH_4 molar conversion. (b) CO_2 molar conversion. (c) H_2 selectivity. (d) CO selectivity. (e) Average δ of $CeO_{2-\delta}$. (f) Solar-to-fuel energy efficiency. Tests were performed at varying inlet $CO_2 : CH_4$ (3 : 1, 3 : 1, 2 : 1, 1.2 : 1) 40% diluted in Ar, and with the packed bed installation in the tubular section.

our definition of $\eta_{\text{solar-to-fuel}}$ given by eqn (6). According to eqn (6), Fosheim *et al.*[24] reported a value of 30%, and Warren *et al.* 17%. Based on an analogous definition but only considering the converted CH_4 in the denominator of eqn (6), Welte *et al.*[20] reported a value of 12%, Warren *et al.*[39] 21%, and we report in this study a peak value of 23% for redox reforming and 42% for the co-feeding mode.

Comparing operating modes

Tests are conducted to directly compare the operating modes of co-feeding and redox reforming. The system is injected with a total flow of 105 L_n min^{-1} under isothermal conditions. First the system is run in co-feeding operation until steady-state conditions are reached. Subsequently, redox reforming cyclic

operation begins with reduction in which the injection times and concentrations are adjusted to mimic that of the co-feed operation. Performing redox reforming cycles directly after the co-feed run ensures a similar δ regime. The two operating modes outline the difference between continuous and batch production of H_2. X_{CH_4} between the co-feed and the respective redox reforming cycle varied by less than 0.05, as the conversions were highly dependent on $T_{nominal}$. Redox reforming cycles displayed X_{CO_2} 0.12 higher than the co-feeding runs which is due to the increased δ caused by the reduction step, thus causing CO_2 conversions to increase. Syngas selectivities between the operating modes varied by less than 0.05 due to the similar operating δ regime. The δ_{mean} for the comparison tests varied by less than 0.008 between the two operation modes, thus validating that they are within the same δ regime. The redox reforming cycles showed higher δ_{mean}, as expected since they follow of the co-feeding runs. $\eta_{solar\text{-}to\text{-}fuel}$ varied significantly between the two operation modes. The redox reforming mode operated at efficiencies (13%) 11 percentage points less than those seen during co-feeding (24%). This is due to the stepwise production of syngas during redox reforming. For this reason, syngas was produced at roughly half the rate as obtained for co-feeding operation, although P_{solar} was maintained at the same level to ensure a constant $T_{nominal}$. With respect to system operation P_{solar} during the co-feeding mode was also easier to control due to a constant endothermic reaction. The redox reforming cycles underwent endothermic and exothermic swings which caused difficulties when controlling $T_{nominal}$.

Conclusions

The experimental campaign has some inherent challenges in obtaining clean and reproducible data, managing molar balances and predicting which reactions are taking place because there are a multitude of different reactions with and without non-stoichiometric ceria. The process runs under isothermal conditions which are difficult to maintain compared to a laboratory setup because of the fluctuating DNI throughout the day and the high reacting gas concentrations ($\leq$40%), which lead to temperature fluctuations due to the endo/exothermic reactions.

The position of the B-Type TCs is behind the RPCs while the inner surface is more susceptible to flux changes and also experiences first contact with the reacting gases. Hence, the nominal reactor temperature as determined by the B-Type TCs may not be indicative of the true reacting temperature. Previous heat transfer modelling of a solar reactor containing a RPC structure indicated significant temperature gradients between the irradiated frontside of the RPC and its backside.[61]

The transients within the system pose a challenge when aiming to achieve steady-state conditions. The thermal insulation and packed bed have high thermal inertia, and therefore take a significant fraction of a testing day to heat up and reach steady-state conditions. The management of the non-stoichiometry has its own challenges. The pure H_2O/CO_2-splitting redox cycle (R3–R5) operates in a Boolean manner between a reduced (at $\delta < 0.05$) and a re-oxidized state. In contrast, due to the reducing agent redox reforming deals with a larger possible δ regime ($\lessapprox$0.345),[26] where a maximum δ is avoided to prevent phase changes. Due to the large variation in δ it is difficult to reproduce tests on another day and pseudo-steady-state conditions may be observed.

Keeping these challenges in mind, the experimental campaign proved successful in demonstrating feasible dry CH_4 reforming in both the redox reforming and co-feeding operation modes using a directly-irradiated solar reactor tested in a solar tower configuration. Across 24 testing days, 12 500 L_n of CH_4 and 27 300 L_n of CO_2 were fed into the reactor, both having average conversions of 31%. This resulted in a total of 15 200 L_n of syngas (*i.e.* H_2 = 3800 L_n, CO = 11 400 L_n).

A parametric study of the redox reforming with high-δ cycles was performed in which nominal temperatures (800–1000 °C) and educt concentrations varied (3, 5, 10, and 20% CH_4/CO_2-Ar). Conversions improved with temperature and maximum CH_4 conversions reached 70%. H_2 selectivities improved with high-δ cycles by 160% reaching a maximum value of 68%. The solar-to-fuel energy efficiency reached 16%. The parametric co-feeding study varied the nominal temperatures (800–1000 °C) and $CO_2:CH_4$ (4 : 1, 3 : 1, 2 : 1, and 1.2 : 1) at 40% diluted in Ar. Conversions improved with temperature reaching a maximum value of 59%, and H_2 selectivities increased with lower $CO_2:CH_4$ reaching a maximum of 71%. The solar-to-fuel energy efficiency peaked at 27%. Overall, the two operation modes run similarly in terms of product compositions. However, the co-feeding mode benefits from continuous production and yields efficiencies approximately twice as high as the redox reforming cycles.

The implementation of a packed bed in the tubular reactor allowed for the use of a morphology with a high SSA. With the packed bed syngas productions improved by 32% by increasing the CeO_2 mass by 22%. Overall, running the redox system in a co-feeding operation mode with a low inlet $CO_2:CH_4$ performs the best due to the continuous syngas production, while mitigating side reactions due to minimal excess CO_2.

Nomenclature

DNI	direct normal irradiance [W m^{-2}]
$\Delta\delta$	change in non-stoichiometry
ΔH	heat of reaction [kJ mol^{-1}]
δ	non-stoichiometry
δ_{eq}	equilibrium non-stoichiometry
δ_{mean}	average non-stoichiometry
δ_{red}	non-stoichiometry in reduced state
δ_o	initial non-stoichiometry
δ_{ox}	non-stoichiometry in oxidized state
$\eta_{solar\text{-}to\text{-}fuel}$	solar-to-fuel energy efficiency [%]
HHV	higher heating value [kJ mol^{-1}]
HV	heating value [kJ mol^{-1}]
L_n	normal liters [L]
M_{CeO_2}	molar mass of ceria, 172.115 [g mol^{-1}]
m_i	mass [g]
n_i	moles [mol]

$\dot{n}i$	molar flowrate [mol s^{-1}]
$\dot{V}i$	volumetric flowrate [L_n min^{-1}]
ν_i	stoichiometric coefficient
P	power [kW]
Q_{solar}	solar radiative energy input through aperture [kJ]
P_{solar}	solar radiative power input through aperture [kW]
ppi	pores per inch [in^{-1}]
RPC	Reticulated porous ceramic
RWGS	reverse water-gas shift
S_k	selectivity of product k [-]
SSA	specific surface area [m^2 g^{-1}]
TC	thermocouple
T	temperature [°C]
$T_{nominal}$	nominal cavity temperature [°C]
$T_{pb,nominal}$	nominal packed bed temperature [°C]
t	time [hh:mm]
X_i	conversion of educt i [-]

Conflicts of interest

Authors have financial interests in Synhelion SA.

Acknowledgements

This work was funded by the Swiss Federal Office of Energy (Project HYBREC – Grant No. SI/501854-01) and by the European Union's Horizon 2020 Research Infrastructure Programme (Project SFERA-III – Grant No. 823802). We acknowledge the support of the Natural Sciences and Engineering Research Council of Canada (NSERC), [PGSD3-545236-2020]. We thank the technical support from the Synhelion team: Marco Gil, Adriano Patané, David Rutz, Gianluca Ambrosetti, and Philipp Good, the IMDEA Energy team: Alejandro Martínez Hernández, Mario Sánchez Redero, the control systems support from Martin Keller, and scientific advice from Brendan Bulfin.

References

1 M. Romero and A. Steinfeld, *Energy Environ. Sci.*, 2012, **5**, 9234–9245.
2 R. Schäppi, D. Rutz, F. Dahler, A. Muroyama, P. Haueter, J. Lilliestam, A. Patt, P. Furler and A. Steinfeld, *Nature*, 2022, **601**, 63–68.
3 S. Zoller, E. Koepf, D. Nizamian, M. Stephan, A. Patané, P. Haueter, M. Romero, J. Gonzalez-Aguilar, D. Lieftink, E. de Wit, S. Brendelberger, A. Sizmann and A. Steinfeld, *Joule*, 2022, **6**, 1606–1616.
4 A. Segal and M. Epstein, *Sol. Energy*, 2003, **75**, 479–490.
5 A. Berman, R. K. Karn and M. Epstein, *Green Chem.*, 2007, **9**, 626–631.
6 R. Diver, J. D. Fish, R. Levitan, M. Levy, E. Meirovitch and H. Rosin, *Sol. Energy*, 1992, **48**, 21–30.
7 R. Buck, J. F. Muir, R. E. Hogan and R. D. Skocypec, *Sol. Energy Mater.*, 1991, **24**, 449–463.
8 J. F. Muir, R. E. Hogan, R. D. Skocypec and R. Buck, *Sol. Energy*, 1994, **52**, 467–477.
9 T. Kodama, T. Shimizu, T. Satoh, M. Nakata and K. I. Shimizu, *Sol. Energy*, 2002, **73**, 363–374.
10 M. Levy, R. Levitan, E. Meirovitch, A. Segal, H. Rosin and R. Rubin, *Sol. Energy*, 1992, **48**, 395–402.
11 S. Wang and L. G. Q. Max, *Energy Fuels*, 1996, **10**, 896–904.
12 A. Worner and R. Tamme, *Catal. Today*, 1998, **46**, 165–174.
13 A. Abdulrasheed, A. A. Jalil, Y. Gambo, M. Ibrahim, H. U. Hambali and M. Y. Shahul Hamid, *Renewable Sustainable Energy Rev.*, 2019, **108**, 175–193.
14 A. Steinfeld, in *Annual Review of Heat Transfer*, Begell House, Inc., 2012, ch. 8, pp. 255–275.
15 M. M. Nair and S. Abanades, *Energy Fuels*, 2016, **30**, 6050–6058.
16 D. Marxer, P. Furler, M. Takacs and A. Steinfeld, *Energy Environ. Sci.*, 2017, **10**, 1142–1149.
17 W. C. Chueh, C. Falter, M. Abbot, D. Scipio, P. Furler, S. M. Haile and A. Steinfeld, *Science*, 2010, **330**, 1797–1801.
18 S. Chuayboon, S. Abanades and S. Rodat, *Chem. Eng. J.*, 2019, **356**, 756–770.
19 K. J. Warren, J. Reim, K. Randhir, B. Greek, R. Carrillo, D. W. Hahn and J. R. Scheffe, *Energy Technol.*, 2017, **5**, 2138–2149.
20 M. Welte, K. Warren, J. R. Scheffe and A. Steinfeld, *Ind. Eng. Chem. Res.*, 2017, **56**, 10300–10308.
21 F. He, J. Trainham, G. Parsons, J. S. Newman and F. Li, *Energy Environ. Sci.*, 2014, **7**, 2033–2042.
22 T. Kodama, H. Ohtake, S. Matsumoto, A. Aoki, T. Shimizu and Y. Kitayama, *Energy*, 2000, **25**, 411–425.
23 P. T. Krenzke, J. R. Fosheim, J. Zheng and J. H. Davidson, *Int. J. Hydrogen Energy*, 2016, **41**, 12799–12811.
24 J. R. Fosheim, B. J. Hathaway and J. H. Davidson, *Energy*, 2019, **169**, 597–612.
25 F. Donat and C. R. Müller, *Appl. Catal., B*, 2020, **278**, 119328.
26 B. Bulfin, L. Hoffmann, L. de Oliveira, N. Knoblauch, F. Call, M. Roeb, C. Sattler and M. Schmucker, *Phys. Chem. Chem. Phys.*, 2016, **18**, 23147–23154.
27 B. Bulfin, S. Ackermann, P. Furler and A. Steinfeld, *Sol. Energy*, 2021, **215**, 169–178.
28 A. Steinfeld, P. Kuhn and J. Karni, *Energy*, 1993, **18**, 239–249.
29 A. Steinfeld and G. Thompson, *Energy*, 1994, **19**, 1077–1081.
30 A. Steinfeld, A. Frei, P. Kuhn and D. Wuillemin, *Int. J. Hydrogen Energy*, 1995, **20**, 793–804.
31 Y. Zheng, K. Li, H. Wang, D. Tian, Y. Wang, X. Zhu, Y. Wei, M. Zheng and Y. Luo, *Appl. Catal., B*, 2017, **202**, 51–63.
32 T. Stroud, T. J. Smith, E. Le Saché, J. L. Santos, M. A. Centeno, H. Arellano-Garcia, J. A. Odriozola and T. R. Reina, *Appl. Catal., B*, 2018, **224**, 125–135.
33 S. Das, J. Ashok, Z. Bian, N. Dewangan, M. H. Wai, Y. Du, A. Borgna, K. Hidajat and S. Kawi, *Appl. Catal., B*, 2018, **230**, 220–236.
34 C. Agrafiotis, H. von Storch, M. Roeb and C. Sattler, *Renewable Sustainable Energy Rev.*, 2014, **29**, 656–682.
35 E. J. Sheu, E. M. A. Mokheimer and A. F. Ghoniem, *Int. J. Hydrogen Energy*, 2015, **40**, 12929–12955.
36 D. S. A. Simakov, M. M. Wright, S. Ahmed, E. M. A. Mokheimer and Y. Román-Leshkov, *Catal. Sci. Technol.*, 2015, **5**, 1991–2016.

37 S. A. M. Said, M. Waseeuddin and D. S. A. Simakov, *Renewable Sustainable Energy Rev.*, 2016, **59**, 149–159.
38 A. Steinfeld, M. Brack, A. Meier, A. Weidenkaff and D. Wuillemin, *Energy*, 1998, **23**, 803–814.
39 K. J. Warren, R. J. Carrillo, B. Greek, C. M. Hill and J. R. Scheffe, *Energy Technol.*, 2020, **8**, 2000053.
40 T. Shimizu, K. Shimizu, Y. Kitayama and T. Kodama, *Sol. Energy*, 2001, **71**, 315–324.
41 J. T. Jang, K. J. Yoon, J. W. Bae and G. Y. Han, *Sol. Energy*, 2014, **109**, 70–81.
42 A. Haeussler, S. Chuayboon and S. Abanades, *AIP Conf. Proc.*, 2020, **2303**, 170009.
43 S. Chuayboon and S. Abanades, *Fuel Process. Technol.*, 2021, **211**, 106572.
44 M. Romero, J. González-Aguilar, A. Sizmann, V. Batteiger, C. Falter, A. Steinfeld, S. Zoller, S. Brendelberger and D. Lieftink, *ISES SWC2019/SHC2019 Conference Proceedings*, 2019.
45 S. Ackermann, M. Takacs, J. Scheffe and A. Steinfeld, *Int. J. Heat Mass Transfer*, 2017, **107**, 439–449.
46 P. Furler, J. Scheffe, D. Marxer, M. Gorbar, A. Bonk, U. Vogt and A. Steinfeld, *Phys. Chem. Chem. Phys.*, 2014, **16**, 10503–10511.
47 E. Koepf, S. Zoller, S. Luque, M. Thelen, S. Brendelberger, J. González-Aguilar, M. Romero and A. Steinfeld, *AIP Conf. Proc.*, 2019, **2126**, 180012.
48 B. Bulfin, M. Miranda and A. Steinfeld, *Front. Energy Res.*, 2021, **9**, 677980.
49 M. Blanco-Muriel, D. C. Alacon-Padilla, T. L. Lopez-Moratalla and M. Lara-Coira, *Sol. Energy*, 2001, **70**, 431–441.
50 E. Koepf, W. Villasmil and A. Meier, *Energy Procedia*, 2015, **69**, 1780–1789.
51 N. Muradov and T. Vezirolu, *Int. J. Hydrogen Energy*, 2005, **30**, 225–237.
52 T. Keipi, H. Tolvanen and J. Konttinen, *Energy Convers. Manage.*, 2018, **159**, 264–273.
53 L. Weger, A. Abánades and T. Butler, *Int. J. Hydrogen Energy*, 2017, **42**, 720–731.
54 G. Maag, G. Zanganeh and A. Steinfeld, *Int. J. Hydrogen Energy*, 2009, **34**, 7676–7685.
55 A. Kogan, M. Kogan and S. Barak, *Int. J. Hydrogen Energy*, 2005, **30**, 35–43.
56 S. Abanades and G. Flamant, *Int. J. Hydrogen Energy*, 2007, **32**, 1508–1515.
57 S. Ackermann, L. Sauvin, R. Castiglioni, J. L. Rupp, J. R. Scheffe and A. Steinfeld, *J. Phys. Chem. C*, 2015, **119**, 16452–16461.
58 D. J. M. Bevan and J. Kordis, *J. Inorg. Nucl. Chem.*, 1963, **26**, 1509–1523.
59 R. Korner, M. Ricken and J. Nolting, *J. Solid State Chem.*, 1989, **78**, 136–147.
60 M. Zinkevich, D. Djurovic and F. Aldinger, *Solid State Ionics*, 2006, **177**, 989–1001.
61 S. Zoller, E. Koepf, P. Roos and A. Steinfeld, *J. Sol. Energy Eng.*, 2019, **141**, 021014.